Generation of heavy ion beams using femtosecond laser pulses in the target normal sheath acceleration and radiation pressure acceleration regimes

G. M. Petrov, C. McGuffey, A. G. R. Thomas, K. Krushelnick, and F. N. Beg

Citation: Physics of Plasmas **23**, 063108 (2016); doi: 10.1063/1.4953546
View online: http://dx.doi.org/10.1063/1.4953546
View Table of Contents: http://scitation.aip.org/content/aip/journal/pop/23/6?ver=pdfcov
Published by the AIP Publishing

Generation of heavy ion beams using femtosecond laser pulses in the target normal sheath acceleration and radiation pressure acceleration regimes

G. M. Petrov,[1,a)] C. McGuffey,[2] A. G. R. Thomas,[3] K. Krushelnick,[3] and F. N. Beg[2]
[1]*Naval Research Laboratory, Plasma Physics Division, 4555 Overlook Ave. SW, Washington, DC 20375, USA*
[2]*Mechanical and Aerospace Engineering and Center for Energy Research, University of California-San Diego, La Jolla, California 92093, USA*
[3]*Center for Ultrafast Optical Science, University of Michigan, Ann Arbor, Michigan 48109, USA*

(Received 22 February 2016; accepted 26 May 2016; published online 10 June 2016)

Theoretical study of heavy ion acceleration from sub-micron gold foils irradiated by a short pulse laser is presented. Using two dimensional particle-in-cell simulations, the time history of the laser pulse is examined in order to get insight into the laser energy deposition and ion acceleration process. For laser pulses with intensity 3×10^{21} W/cm^2, duration 32 fs, focal spot size 5 μm, and energy 27 J, the calculated reflection, transmission, and coupling coefficients from a 20 nm foil are 80%, 5%, and 15%, respectively. The conversion efficiency into gold ions is 8%. Two highly collimated counter-propagating ion beams have been identified. The forward accelerated gold ions have average and maximum charge-to-mass ratio of 0.25 and 0.3, respectively, maximum normalized energy 25 MeV/nucleon, and flux 2×10^{11} ions/sr. An analytical model was used to determine a range of foil thicknesses suitable for acceleration of gold ions in the radiation pressure acceleration regime and the onset of the target normal sheath acceleration regime. The numerical simulations and analytical model point to at least four technical challenges hindering the heavy ion acceleration: low charge-to-mass ratio, limited number of ions amenable to acceleration, delayed acceleration, and high reflectivity of the plasma. Finally, a regime suitable for heavy ion acceleration has been identified in an alternative approach by analyzing the energy absorption and distribution among participating species and scaling of conversion efficiency, maximum energy, and flux with laser intensity. *Published by AIP Publishing*. [http://dx.doi.org/10.1063/1.4953546]

I. INTRODUCTION

Short pulse lasers have been extensively used for generation of intense multi-MeV ion beams, especially protons. For many years, the increase in maximum energy and conversion efficiency into protons and heavier ions has been incremental. Recently, the laser technology and target preparation techniques have experienced marked improvement, setting the stage for a leap in laser-driven ion acceleration. Clean laser pulses with intensity $I > 10^{21}$ W/cm^2 and ultrathin (nm) targets are now available and have been used in a number of experiments, making long-standing predictions of advanced acceleration schemes verifiable. The Target Normal Sheath Acceleration (TNSA)[1] has been the hallmark of ion acceleration for nearly two decades, but it is now possible to go beyond TNSA and reach more favorable regimes. In recent years, a number of ion acceleration schemes such as Radiation Pressure Acceleration (RPA) in circular[2–5] and linear[6,7] polarizations, "laser-piston" (LP),[8] Relativistic Induced Transparency (RIT),[9] shock acceleration,[10] and Breakout Afterburner (BoA)[11] have been defined theoretically and studied in a large number of works. In spite of the different names and physical description such as "laser-piston," "light sail (LS)," "radiation pressure," and "shock acceleration," many of them share similar properties and have their roots in a fundamental process of pushing a slab of quasi-neutral plasma in a piston-like fashion.[8] On the experimental side, transition from TNSA to RPA[12] and BoA[13,14] for protons and carbon ions has been demonstrated. The advances in laser technology, the most prominent of which is ultra-high contrast laser pulses allowing the utilization of nanometer-scale targets, are currently marked with impressive results: 40 MeV protons from a laser system with only 7.5 J of laser energy on target,[15] C_6^+ ions with energies exceeding 80 MeV/nucleon[14] and ~1 GeV fully stripped Fe ions,[16] to name a few.

In all these studies, the focus was on protons and light ions, for which the above mentioned acceleration mechanisms have been attributed. Mid-Z ions were also investigated,[16–18] while for heavy ions (W, Au, etc.), only a handful of experimental[19,20] and theoretical studies[21,22] exist. No acceleration mechanisms have been identified for mid- and high-Z ions. Braenzel *et al.*[20] developed an analytical model to elucidate the steep dependence of the maximum energy of gold ions as a function of ion charge, but the exact acceleration process remains unknown. The matter is even more complicated since these ions can originate from different parts of the target: bulk[17,18] or from a thin layer on the rear surface of the foil, akin to contaminants.[16] This implies that different acceleration mechanisms can be at play depending on the location of ions of interest in the target (bulk or surface). With a plethora of experimental and theoretical studies devoted to protons and light ions, the next logical step is to extend the research to the more challenging case of heavy ions such as Au or W. It is of fundamental interest to understand the intricate details and issues relevant to heavy ion beam acceleration. The present study has been motivated by

a)E-mail: george.petrov@nrl.navy.mil

three factors, which come together as a results of recent breakthroughs in laser development and theoretical advancements in the field: (i) the issues and physics of heavy ion acceleration are unknown; (ii) the laser and target parameter landscape has not been mapped, e.g., it is unknown what combination of laser systems and targets will work best; and (iii) the availability of ultra-high contrast lasers ($>10^{10}$) and ultrathin foils (down to 5–10 nm), which allow the exploration of a wide variety of ion acceleration mechanisms.

The paper is arranged with an analytical portion (Sections II and III) and a modeling and simulations portion (Sections III and IV). In Section II, we review the requirements and challenges facing the acceleration of heavy ions. In Section III A, we map the ion acceleration mechanisms versus foil thickness. An example of heavy ion acceleration in the RPA regime is presented in Section III B, where numerical simulations for gold ion acceleration from sub-micron foils are carried out using a 2D3V particle-in-cell (PIC) code. Analogous results in the TNSA regime are presented in Section III C. In Section IV, the ion acceleration is analyzed in terms of energy absorption and partition. The conversion efficiency scaling of gold and contaminant ions with laser intensity is investigated. Section V discusses numerical issues pertinent to heavy ion acceleration. A summary of the results is given in Section VI of the paper.

II. CHALLENGES FOR HEAVY ION ACCELERATION

We commence this section by outlining the relevant issues, as well as the conditions appropriate for acceleration of heavy ions. Compared to protons and light ions, the acceleration of heavy ions faces additional restrictions. The major differences between heavy and light ions are:

- Lower charge-to-mass ratio: Unlike light ions, heavy ions cannot be fully stripped by collisional and optical field ionization by laser pulses commonly used nowadays (sub-picosecond, laser intensity $<10^{22}\,\mathrm{W/cm^2}$). The maximum ion charge that can be reached by ionization is well below the theoretical maximum (the element atomic number). It will be shown that the maximum charge-to-mass ratio $(q/M)_{\max}$ for heavy ions is roughly half the maximum charge-to-mass ratio for light ions, which implies lower maximum energy and stiff competition between the heavy ions and the ever-present contaminants on the target surface.
- Fewer ions available for acceleration: Only those residing in or near the focal spot can reach high charge-to-mass ratio and can be efficiently accelerated.
- Delayed acceleration: Heavy ions can be efficiently accelerated only once high charge state is reached by Optical Field Ionization which does not occur until near or after the peak of the laser pulse.
- Plasma mirror effect: Due to the large ion charge in the focal spot ($q \cong 50$), the electron density becomes extremely high, exceeding 2000 times the critical electron density right at the moment the ion acceleration starts. Most of the laser pulse is reflected, reducing coupling to the target.

The most critical issue facing heavy ion acceleration is the low charge-to-mass ratio q/M, since the normalized ion energy scales as $E/M \sim (q/M)^2$.[20,23,24] The charge-to-mass ratio is lower for heavy materials because of excess neutrons, e.g., excess mass, as well as higher ionization potentials. For gold, the estimated maximum ion charge and charge-to-mass ratio are $q \cong 70$ and $(q/M)_{\max} \cong 0.35$, respectively. For convenience, throughout the paper, the mass M in the charge-to-mass ratio is taken in proton units. This is illustrated in Figure 1, where the maximum charge-to-mass ratio is plotted versus laser intensity. It is based on the so-called Bethe rule, $I_{th} = \frac{2.2\times10^{15}}{\bar{z}^2}\left(\frac{I_p(\bar{z})}{27.21}\right)^4$, which relates the threshold laser intensity I_{th} (in units [W/cm^2]) for optical field ionization to the maximum reachable charge $\bar{q} = \bar{z} - 1$ of ion having ionization potential $I_p(\bar{z})$ (in units [eV]).[25,26] In reality, the most likely ion charge and charge-to-mass ratio for Au ions are $q \cong 50$ and $q/M \cong 0.25$, respectively, as it will be shown later with simulations. From Figure 1, we conclude that laser intensities below about $I \sim 10^{20}\,\mathrm{W/cm^2}$ are inadequate for heavy ion acceleration. The low q/M is disadvantageous for Au and entails the well-known "contaminants problem": a thin (2–3 nm) layer of hydrocarbon or water residing on the surface of the foil steals nearly all the energy coupled to the plasma and suppresses the acceleration of heavy ions. This effect has already been seen experimentally for mid-Z ions.[17,18] It is worth noting that for sub-picosecond pulses, collisional ionization does not increase the ion charge appreciably and has a minor impact on the results shown in Figure 1.

The second problem is the limited number of heavy ions that can be accelerated. Since q/M is very sensitive to I, the only useful ions amenable to acceleration reside in the laser focal spot. This is in contrast to low-Z ions, e.g., carbon, which can be fully ionized at much lower intensities, and the available ions for acceleration extend into the wings of the laser intensity profile. Since the number of atoms in the foil scales with distance from focal spot center as r^2, we estimate that the number of gold ions that can be efficiently accelerated is at least one order of magnitude less than the corresponding number of carbon ions and protons.

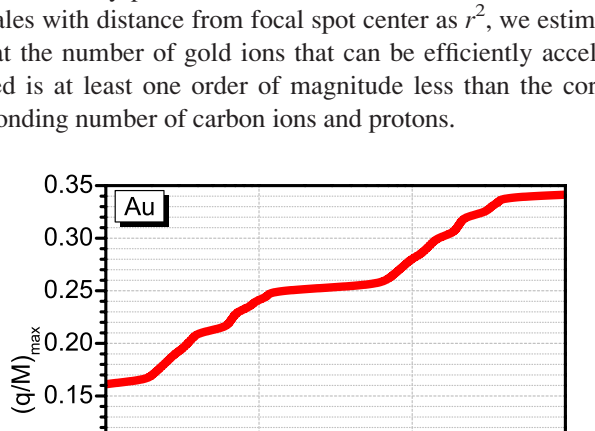

FIG. 1. Maximum charge-to-mass ratio for gold ions vs. peak laser intensity. Only optical field ionization is accounted for. Collisional ionization is neglected.

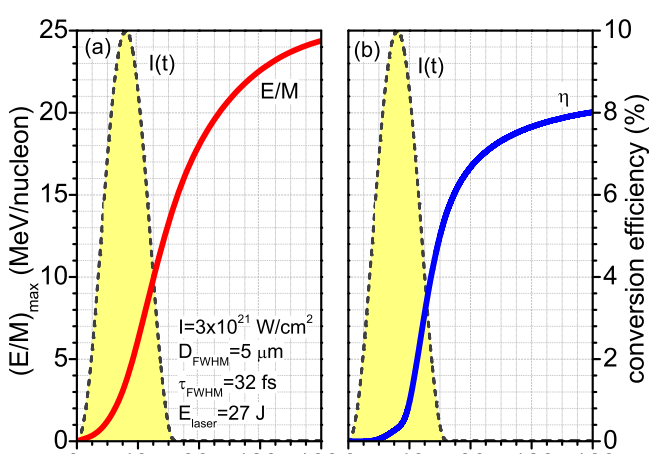

FIG. 2. Maximum energy (a) and conversion efficiency into gold ions (b) vs. time. The yellow shaded area is the laser pulse profile. The laser and foil parameters are listed in Table I.

The third issue is more subtle and is unique for heavy ions. Ionization and acceleration are divided into two distinct phases separated in time, e.g., a phase of ionization and a phase of acceleration. During the first phase, the ions must be ionized to very high charge states, a process that terminates at the peak of the laser pulse. The second phase, acceleration, takes place during the pulse fall-off, shortening the time available for acceleration by a factor of two. The two phases are shown in Figure 2 aided by 2D PIC simulations. The laser pulses and foil parameters are listed in Table I. The maximum ion energy and conversion efficiency into gold ions increase sharply, but only after the peak of the laser pulse. The ion acceleration is "delayed" until the laser pulse reaches its peak, and only half of the pulse can be used to accelerate ions, which may prevent ions from reaching full velocity. Thus, short laser pulses (30–40 fs), which are attractive for acceleration of light ions, are borderline adequate for heavy ions due to insufficient acceleration time. This drawback can be compensated by increasing the laser intensity, which once again leads to the conclusion that high intensities are required.

The fourth issue is the high reflectivity of the target. Ion acceleration commences at the peak of the laser pulse, when the ion charge state is already high (Figure 2). The electron density reaches values on the order of $n_e \cong \bar{q} n_{Au} \cong 3 \times 10^{24}\,\mathrm{cm}^{-3}$, which results in a plasma that is $n_e/n_{cr} > 2000$ times overdense (n_{cr} is the critical density). The "plasma mirror" reflects most of the incoming laser radiation (cf. Figure 8, line denoted as ε^{out}), reducing coupling of laser energy to ions.

Another potential problem is the finite laser pulse contrast. Poorly controlled pre-pulses can ablate material or launch high velocity (a few km/s) shock wave, which propagates through the target causing severe damage and deformation. In this work, we assume high-contrast laser pulses having pre-pulses below the damage threshold of the material. For Au, the damage threshold for picosecond pulses is ~0.5 J/cm^2,[27] which for a ~5–50 ps pre-pulse corresponds to threshold intensity on the order of $I_{thr} \cong 10^{10}$–$10^{11}\,\mathrm{W/cm}^2$. For the laser intensities considered in this work, the pre-pulse contrast should be better than 10^{10}.

TABLE I. Laser, target, and computational domain parameters used in the simulations.

Parameter	Variable and units	Value
Laser intensity	$I_0\,(\mathrm{W/cm}^2)$	3×10^{21}
Pulse duration	τ_{FWHM} (fs)	32
Focal spot size	D_{FWHM} (μm)	5
Wavelength	λ (μm)	0.8
Energy	ε_{laser} (J)	27
Foil thickness	L (nm)	20
Foil width	W (μm)	126
Computational domain	$L_x \times L_y\,(\mu\mathrm{m}^2)$	100×128
Cell size	$\Delta x \times \Delta y\,(\mathrm{nm}^2)$	20×20
Time step	$\Delta t\,(\lambda/c)$	0.005
Simulation time	t_{sims}(fs)	320

III. ACCELERATION MECHANISMS FOR HEAVY ION BEAMS

A. The RPA and TNSA regimes in the short pulse laser limit

One of the advanced acceleration schemes exhibiting superior scaling is RPA, which works for both circular and linear polarization.[6,7] The concept was developed by Esirkepov *et al.* for acceleration of ions from ultrathin foils to relativistic energies.[21] The laser energy can be transformed efficiently into ion kinetic energy when the radiation pressure is dominant. For RPA to work, the target must remain overdense for the duration of the pulse, which implies the use of short (30–50 fs) laser pulses. Laser pulses with longer pulse duration (a few hundred femtoseconds) cannot keep the plasma overdense due to plasma expansion, which leads to a different ion acceleration mechanism (BoA[11]). In addition, in the "thin foil" regime, the hole-boring (HB) process must reach the rear of the foil before the laser pulse ends, which imposes limitations on the foil thickness. We selected a range of peak laser intensities, $3 \times 10^{20} < I_0 < 3 \times 10^{21}\,\mathrm{W/cm}^2$, suitable for RPA and in accordance with Figure 1. We will begin by introducing a useful scale length and relate other parameters such as foil thickness to it. Perhaps the most important one is the relativistic skin depth, $\ell_{skin} = \gamma^{1/2} c/\omega_p$, where γ and ω_p are the relativistic parameter and electron plasma frequency, and c is the speed of light. For simplicity, γ and ω_p are taken at the peak of the laser pulse. The skin depth is chosen because it is convenient (comparable to foil thickness), separates "transparent" from "opaque" foils, and the energy absorption reaches maximum for foil thickness comparable to the skin depth. After a few simple mathematical manipulations, the skin depth takes the form

$$\ell_{skin} = \left(\frac{\gamma n_{cr}}{n_e}\right)^{1/2} \frac{\lambda_0}{2\pi}. \tag{1}$$

The right hand side of (1) scales weakly with peak laser intensity, $\ell_{skin} \sim \gamma^{1/2} \cong a_0^{1/2} \sim I_0^{1/4}$. For typical laser and plasma parameters in the focal spot, $\gamma \cong 12$–37, $\bar{q} \cong 50$,

$n_e \cong \bar{q} n_{Au} \cong 3 \times 10^{24}\,\mathrm{cm}^{-3}$, and $n_{cr} \cong 1.8 \times 10^{21}\,\mathrm{cm}^{-3}$, formula (1) yields $\ell_{skin} \cong (0.014\text{–}0.024)\lambda_0 \cong 11\text{–}20\,\mathrm{nm}$, where λ_0 is the laser wavelength (typically either 0.8 or 1.06 μm).

The second parameter of importance for RPA is the optimal foil thickness ℓ^{opt} derived from the condition $\frac{n_e}{n_{cr}}\frac{\ell^{opt}}{\lambda_0} \cong a_0$,[4,6,28,29] stating that the normalized areal density is equal to the normalized laser field amplitude $a_0 = 8.5 \times 10^{-10}\sqrt{I_0}\lambda_0$. In the above formulas, I_0 is in units W/cm^2 and λ_0 is in units of μm. This formula was first proposed by Esirkepov *et al*. who conducted a large-scale parametric study by varying laser and target parameters and determined that in the framework of RPA maximum ion energy is reached for optimal target aerial density $\sigma^{opt} = n_e \ell^{opt} \cong 0.4 a_0 n_{cr} \lambda_0$.[30]

Using formula (1), it can be written in an alternative form

$$\frac{\ell^{opt}}{\ell_{skin}} \cong \frac{4\pi\ell_{skin}}{\lambda_0}. \tag{2}$$

For high-Z material, the right hand side is between 0.2 and 0.3, e.g., the optimum foil thickness for gold in the RPA regime is 1/4 of the relativistic skin depth. For foil thickness $L \le \ell^{opt}$, the RPA is unstable with all electrons blown out of the foil. For stable RPA, the foil thickness must be larger than the "optimal thickness" given by Equation (2).

The third scale length of importance is the hole-boring length $\ell_{HB} = \mathrm{v}_{HB}\tau_{HB}$, which divides the RPA into hole-boring (HB) and light sail (LS) regimes.[28,29] The normalized hole-boring velocity, $\frac{\mathrm{v}_{HB}}{c} = \sqrt{\frac{\bar{q}}{M}\frac{m_e}{m_p}\frac{n_{cr}}{n_e}}a_0$,[28,29] is the recession velocity of the plasma surface driven by the laser piston. The difference between light and heavy ions becomes immediately apparent considering the scaling with ion mass, $\mathrm{v}_{HB} \sim M^{-1/2}$. The hole-boring velocity for gold is four times slower compared with that for carbon. To be effective, the hole boring should occur during the laser pulse duration, e.g., $\tau_{HB} \cong \tau_{FWHM}$. In order to accelerate ions in the RPA-LS regime, $L < \ell_{HB}$ is required. Using again the expression for the skin depth (1), the hole-boring length can be written as $\ell_{HB} = \sqrt{\frac{\bar{q}}{M}\frac{m_e}{m_p}}2\pi N_{laser} a_0^{1/2}\ell_{skin}$. Combining the two conditions, $L > \ell^{opt}$ for stable RPA, and $L < \ell_{HB}$ for LS-RPA, we arrive at

$$\frac{4\pi\ell_{skin}}{\lambda_0} < \frac{L}{\ell_{skin}} < \sqrt{\frac{\bar{q}}{M}\frac{m_e}{m_p}}2\pi N_{laser} a_0^{1/2}. \tag{3}$$

The right hand side of (3), assuming charge-to-mass ratio $\frac{\bar{q}}{M} \cong \frac{1}{4}$, number of laser periods $N_{laser} = \frac{c\tau_{FWHM}}{\lambda_0} = 12$ and $a_0 \cong 12\text{–}37$, is between 4 and 6. Thus, for a typical short pulse laser (30–40 fs), the foil thickness in the RPA-LS regime is limited in the interval

$$\frac{1}{4}\ell_{skin} < L < 5\ell_{skin}. \tag{4}$$

In absolute units, it is between 5 and 100 nm. This range is extended for longer pulse duration. Equation (4) is simple and has a clear physical meaning: RPA-LS is realized for foil thickness comparable to the skin depth. All ions in the focal spot can be volumetrically accelerated, which is very efficient and optimizes the energy absorption.[11,31] Another advantage of using formula (3) or (4) for crude estimates is that both sides scale weakly with laser intensity, $\sim I_0^{1/4}$.

The regime landscape is illustrated schematically in Fig. 3. Acceleration from foils that are too thin such that $L < \frac{1}{4}\ell_{skin}$ is inherently unstable and corresponds to the Coulomb Explosion (CE) regime.[32] For foil thickness obeying $\frac{1}{4}\ell_{skin} < L < 5\ell_{skin}$, the ion acceleration is formally in the RPA-LS regime, and for $L > 5\ell_{skin}$, the conventional TNSA takes place. For full dominance of RPA over TNSA, it is also required that the maximum velocity of the ions (about twice the hole-boring velocity) exceeds the maximum ion velocity obtained by TNSA.[6]

B. Numerical simulations of heavy ion acceleration in the RPA regime

Numerical simulations for gold ion acceleration in the RPA regime are performed using a two-dimensional electromagnetic PIC code.[33,34] The target is a flat 20 nm Au foil covered with a 5 nm contaminant layer residing on the back of the foil, located at spatial position $x = 48\,\mu$m. For numerical purposes, the contaminants are modeled as a thin sheet of water at liquid density. The foil thickness is chosen to roughly correspond to the relativistic skin depth. Under these conditions, the laser field can penetrate the whole target and volumetrically accelerate all gold ions in the laser spot. The laser, target, and simulation parameters are listed in Table I. The laser pulse propagates in the "+x" direction and is linearly polarized in the "y" direction. The laser intensity is $\sin^2$ in time and Gaussian in space, $I(t,y) = I_0 \sin^2(\pi t/2\tau_{FWHM})\exp(-(y/r_0)^2)$, having radius $r_0 = \frac{1}{2\sqrt{ln(2)}}D_{\mathrm{FWHM}}$ at 1/e level. The laser energy is calculated according to $\varepsilon_{laser} = \pi r_0^2 I_0 \tau_{\mathrm{FWHM}} \cong 1.13 D_{FWHM}^2 I_0 \tau_{\mathrm{FWHM}}$. The focal spot size D_{FWHM} must be carefully chosen. Additional simulations showed an increase in laser energy coupling to ions with D_{FWHM} increasing steeply for $D_{\mathrm{FWHM}} < 5\,\mu$m, and more gently for $D_{\mathrm{FWHM}} > 5\,\mu$m. We adopted the value of 5 μm. Particles are initialized with charge +1 for ions and −1 for electrons. During the simulations, the ion charge of oxygen and gold is dynamically incremented using a standard Monte Carlo scheme for collisional and optical field ionizations.[35,36] Recombination is neglected since for sub-picosecond pulse at high laser intensities (above about 10^{20}W/cm^2), the corresponding rate is typically lower compared to collisional and optical field ionization rates.[36] Photoionization by x-rays generated during the interaction has also been neglected, but they can be very efficient in increasing the ion charge when "bottleneck is reached" and the ion

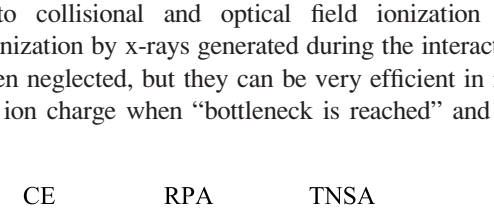

FIG. 3. A sketch of the ion acceleration mechanisms versus foil thickness.

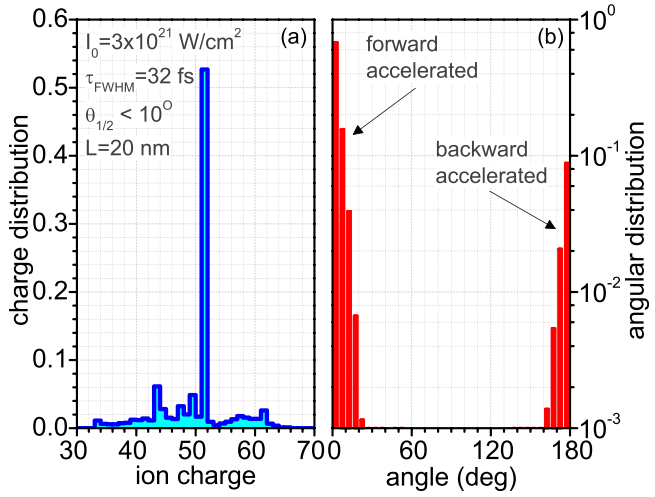

FIG. 4. Charge distribution within solid angle $d\Omega = 0.095$ sr (a) and angular distribution (b) of energetic (>100 MeV) gold ions at the end of the simulations in the RPA regime. The angular bins are every 5°. The laser and foil parameters are listed in Table I. Foil thickness $L = 20$ nm.

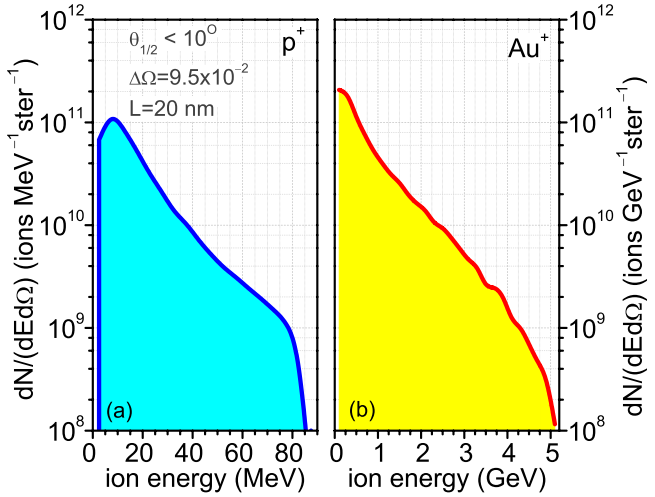

FIG. 5. Energy spectra in the forward direction of energetic gold ions (>0.5 MeV/nucleon) (a) and protons (b) at the end of the simulations in the RPA regime. Only ions with energy within solid angle $d\Omega = 0.095$ sr are shown. The laser and foil parameters are listed in Table I. Foil thickness $L = 20$ nm.

charge stalls.[37] At the beginning of the simulations, the number of particles per cell is ~60 for electrons, gold ions, and protons, and ~30 for oxygen ions. Both the foil material and contaminants are taken at their actual density at room temperature (19.3 and 1 g/cm^3, respectively) without reduction.

We focus on the most important ion beam properties, specifically charge distribution, angular distribution and flux in the forward direction. The charge distribution of Au ions, shown in Figure 4(a), is presented only considering ions with energy >100 MeV (>0.5 MeV/nucleon) and momentum vector within 10 degrees half-angle from the target normal, corresponding to solid angle $d\Omega = 0.095$ sr. The maximum and average charge-to-mass ratios for these ions are 0.3 and 0.25, respectively. Optical field ionization stalls at ion charge 51, and as a result, about half of the ions pile up at $q = 51$, which corresponds to $q/M \cong 0.25$. Only a small fraction of ions with $0.25 < q/M < 0.3$ is observed. The angular distribution is highly peaked, which leads to a large flux in the forward direction. Among all the ions, most ions lie in a cone of ~20° from the target normal (Figure 4(b)). There is a group of ions scattered backward, presumably from Coulomb explosion of the Au layer. According to the simplified theory of RPA, the ions located initially in the compression layer will undergo RPA and will be snow-plowed forward because for these ions the electrostatic pressure balances the radiation pressure, while the plasma containing a sheath of bare ions in the electron depletion layer will Coulomb explode launching ions in the backward direction.[4] It is interesting to note that both forward accelerated and backward scattered ions have very narrow angular distributions, i.e., both are emitted perpendicular to the foil surface. The spectra of protons and gold ions in the forward direction, $\frac{d^2N}{dEd\Omega}$, are plotted in Figure 5. For both protons and gold ions, the cut-off energy is $E/M > 0.5$ MeV/nucleon and only ions moving in a solid angle $d\Omega = 0.095$ sr are collected. The maximum proton energy is 85 MeV. The calculated ion fluxes and maximum energy per nucleon in the forward direction are listed in Table II. The normalized maximum ion energy for gold, oxygen, and protons increases with q/M; however, this increase is closer to linear: $(E/M)_{max} \sim q/M$, rather than quadratic as it was previously found. The most likely reason for the change in scaling is the different and more efficient ion acceleration mechanism, RPA. Numerical simulations show that in the RPA regime, different types of ions can co-propagate and have comparable velocities, which is proportional to q/M.[38]

C. Numerical simulations of heavy ion acceleration in the TNSA regime

Analogous numerical simulations are performed in the TNSA regime by increasing the foil thickness to 200 nm. The charge distribution of forward accelerated gold ions is shifted toward lower charges between 30 and 50 (Figure 6(a)). Now about 75% of these ions have charges lower than the bottleneck value $q = 51$. None of these ions have charge $q > 51$. However, according to Figure 1, ions with charges $51 < q < 60$ should be created in the focal spot directly by optical field ionization from the laser pulse. Figure 6(b) indicates that just like in the RPA regime, there are two groups of counter-propagating ions, one in the forward and another in the backward directions. We looked for the "missing ions" in the backward direction. Indeed, the latter contained a group of ions with charges $q > 51$. The only plausible

TABLE II. Calculated flux, average charge-to-mass-ratio, and maximum energy per nucleon in the forward direction for protons, oxygen, and gold ions. Only ions with energy > 100 MeV within 10° half-angle from the target normal ($d\Omega = 0.095$ sr) are included. The laser and foil parameters are listed in Table I.

Parameter	Protons	O ions	Au ions
$dN/d\Omega$	2.2×10^{12}	3.8×10^{11}	1.7×10^{11}
$\bar{q}/M$	1	0.5	0.25
$(E/M)_{max}$	85	40	25

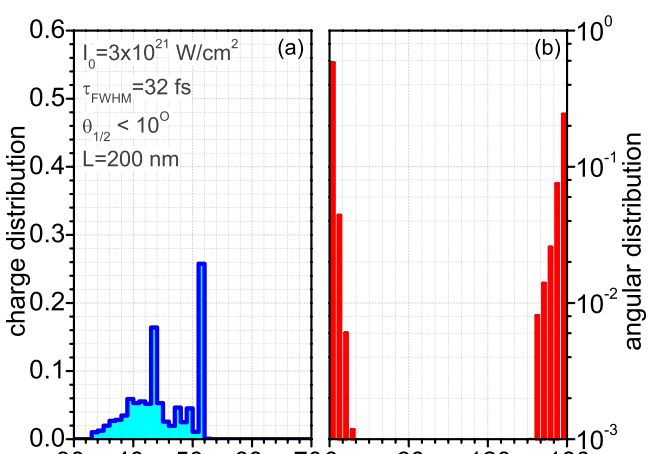

FIG. 6. Charge distribution within solid angle $d\Omega = 0.095$ sr (a) and angular distribution (b) of energetic (>100 MeV) gold ions at the end of the simulations in the TNSA regime. The angular bins are every 5°. The laser parameters are listed in Table I. Foil thickness $L = 200$ nm.

explanation is that ions with charges $51 < q < 60$ are created in the focal spot within one skin layer by optical field ionization from the laser pulse, but instead of being accelerated forward, are moving in the opposite direction driven by Coulomb explosion of unbalanced charges. The ions on the rear side are accelerated forward by TNSA, but the electrostatic field of the sheath is lower than the laser field; therefore, the ion charge stalls at $q = 51$. The "bottleneck" can be overcome considering that at high laser intensities copious amounts of x-rays are generated, as shown by Esirkepov *et al.*,[37] which can further photoionize and increase the ion charge above $q = 51$. The spectra of protons and gold ions in the forward direction are plotted in Figure 7. The proton spectrum is nearly identical to that in Figure 5(a). Protons appear to be mildly affected by target thickness variation and regime of ion acceleration. The spectrum of gold ions has an

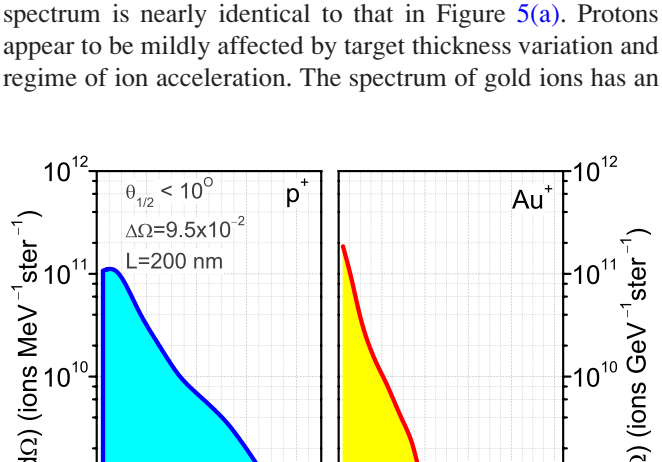

FIG. 7. Energy spectra in the forward direction of energetic gold ions (>0.5 MeV/nucleon) (a) and protons (b) at the end of the simulations in the TNSA regime. Only ions with energy within solid angle $d\Omega = 0.095$ sr are shown. The laser parameters are listed in Table I. Foil thickness $L = 200$ nm.

exponential distribution very similar to that in Figure 5(b), but the maximum energy is only 2 GeV (10 MeV/nucleon).

Comparing the two different target thickness case based on ion beam parameters alone shows that the thinner case is preferable, though they were similar overall (Figure 4 vs. Figure 6 and Figure 5 vs. Figure 7). A more detailed examination, however, reveals different mechanisms of acceleration. In the thin case, exhibiting RPA, gold ions in the skin layer are ionized to very high charge states (~60), then pushed by the laser piston and form the forward-directed beam. In contrast, in the thicker case dominated by TNSA, these ions are blown backward, while the forward moving ions originate from the sheath on the rear surface.

IV. HEAVY ION ACCELERATION MECHANISM: ENERGY CONSIDERATIONS

Though the acceleration mechanism of heavy ions can be formally attributed to the well-known ones discussed in Section I (RPA, BoA, TNSA, etc.), it is instructive to discuss it from a different perspective: energy absorbed by the plasma from the incoming laser pulse and how it is partitioned. The reasoning for adopting this approach is straightforward: regardless of the particular acceleration mechanism, in order to make the acceleration of heavy ions more efficient, one has to maximize the energy absorption and manipulate it by channeling more energy into the desired species (in this case, gold ions). The energy absorption and partition is of fundamental interest and the key to ion acceleration. Therefore, the objectives explored in this section of the paper center on investigating the laser energy deposition into the target. Figure 8(a) shows the global (integrated over the computational domain) energy balance, which at any given time reads

$$\varepsilon^{in}(t) = \varepsilon^{field}(t) + \varepsilon^{out}(t) + \varepsilon^{kin}(t). \quad (5)$$

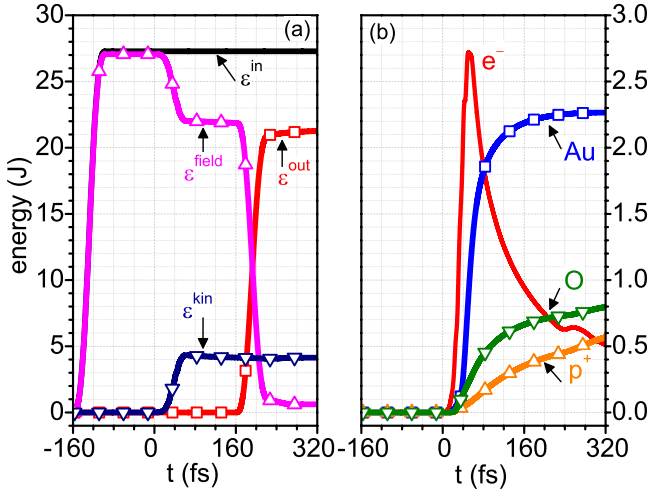

FIG. 8. (a) Energy balance components in Equation (1) versus time: energy entering the computational domain ε^{in}, energy leaving the computational domain ε^{out}, electromagnetic field energy ε^{field}, and kinetic energy ε^{kin}. Time $t_0 = -160$ fs corresponds to the moment the laser pulse enters the computational domain and time $t = 0$ fs is the moment the laser pulse reaches the target. (b) Energy absorption by electrons and ions versus time. The laser and foil parameters are listed in Table I.

The electromagnetic wave energy which entered the computational domain prior to time t, $\varepsilon^{in}(t) = H\int_{t_0}^{t}\int_0^{L_y} I(y,t')dydt'$, is balanced by the electromagnetic field energy $\varepsilon^{field}(t) = \frac{H}{2}\int_0^{L_x}\int_0^{L_y}(\varepsilon_0\vec{E}^2(x,y) + \vec{B}^2(x,y)/\mu_0)dxdy$ residing in the computational domain, electromagnetic energy $\varepsilon^{out}(t) = H\int_{t_0}^{t}\oint_L \vec{S}(t)\cdot\vec{n}d\ell$ that has exited the computational domain, and species kinetic energy $\varepsilon^{kin}(t) = \sum_\beta \varepsilon_\beta$, summed over the kinetic energies of all computational particles β, including those that have left the computational domain. The notation $\vec{n}$ stands for unit vector pointing outward and $\vec{S} = \frac{1}{\mu_0}\vec{E}\times\vec{B}$ is the electromagnetic energy flux (Poynting vector). The laser energy lost for optical field ionization is <0.1% and is not further considered in the paper. The parameter $H = \sqrt{\pi}r_0$ introduced in Ref. 39 allows for transition from energy per unit length to energy. Time $t_0 = -160$ fs corresponds to the moment the laser pulse enters the computational domain at spatial position $x = 0$, and time $t = 0$ is the moment it reaches the target. For time $t \le 0$ $\varepsilon^{field}(t) = \varepsilon^{in}(t)$, i.e., the energy entering the computational domain stays as energy of the electromagnetic field since there is no interaction with the target. At time $t = 0$, the laser pulse reaches the foil. Shortly thereafter, within 1–2 laser cycles, a hot and highly overdense plasma is formed within the target, which gradually increases to density in excess of 10^3 times the critical electron density $n_{cr} \cong 1.8\times10^{21}$ cm^{-3}. Part of the electromagnetic pulse is reflected from the plasma mirror and turns around, while the transmitted part couples energy to the plasma. As a result, for $t > 0$, ε^{field} starts to decrease, while ε^{kin} starts to increase. The sum of the two equals the laser energy that entered the computation domain prior to time t, i.e., $\varepsilon^{field}(t) + \varepsilon^{kin}(t) = \varepsilon^{in}(t)$. Later in time, at $t = 160$ fs, the reflected pulse going in the $-x$ direction reaches the computational domain edge ($x = 0$) and starts to leave. This is seen as a sharp increase in ε^{out} and a corresponding decrease in ε^{field}. The peak of ε^{out} can be used to estimate the reflection coefficient of the plasma, $\xi^r = \varepsilon^{out}(t_{sims})/\varepsilon^{laser}$, while the minimum of ε^{field} can be used to calculate the transmission coefficient $\xi^t = \varepsilon^{field}(t_{sims})/\varepsilon^{laser}$. The simulations show that $\xi^r \cong 80\,\%$ of the laser energy is reflected and completely lost, $\xi^t \cong 5\,\%$ is transmitted through the target and the remaining 15% is coupled to the plasma. The small transmission coefficient indicates that during the acceleration process the plasma remains opaque, consistent with the definition for RPA. The reflectivity of the target is a combination of two factors. The first one stems from the assumption of ultrahigh laser contrast, which implies sharp front surface and no pre-plasma that absorbs energy at the "critical density." The second factor leading to high plasma reflectivity is the large average ion charge $\bar{q} \cong 50$ leading to highly overdense plasma $n_e \cong \bar{q}n_{Al} \sim \bar{q}$, which acts as a "mirror." The individual terms of the energy balance are plotted in Figure 8(a). Due to imperfections in the numerical discretization, formula (5) is not exactly fulfilled. A small fraction (a few percent) of the energy "leaks" (i.e., lost) since the numerical procedure does not ensure exact energy conservation,[39] unless it is artificially enforced.[40] This is acceptable, keeping in mind that the simulations are computationally very intensive, but the relative error in the energy balance can be controlled by reducing the time step and/or increasing the number of computational particles.[39]

Of primary interest to our investigation is the laser energy converted into species kinetic energy. The kinetic energy increases during the pulse ($0 \le t \le 2\tau_{FWHM}$) and then levels off. About 4 J worth of laser energy is converted into kinetic energy, which is ~15% of the laser energy on target. This energy is distributed among the species: electrons (1.9%), gold ions from the bulk (8.3%), protons (2.1%), and oxygen ions (2.9%) from the contaminant layer. Figure 8(b) plots the time evolution of energy absorbed by individual species. At the end of the simulations, more energy has been coupled to Au compared to both oxygen and protons. At these conditions, the contaminants are no longer a problem. This is accomplished due to the appropriate choice of laser and target parameters. Next, we investigate the coupling efficiency as a function of laser intensity. As is well known, in the limiting case of low intensities, the laser energy is coupled exclusively to the contaminants, more specifically, protons. In the other extreme of very high intensity, such as the case plotted in Figure 8, the opposite happens. One can argue that there is a critical laser energy/intensity, below which the contaminants "win" and above which lies the regime suitable for heavy ion acceleration. An intensity scan was conducted to pinpoint the critical laser intensity.

Simulation results are plotted in Figure 9 for peak laser intensities between 5×10^{20} W/cm^2 and 3×10^{21} W/cm^2. The laser energy varies from 4.5 to 27 J. The total and individual conversion efficiencies into ions η are plotted in Figures 9(a) and 9(b). With laser intensity increasing the conversion efficiency into protons and oxygen ions stays flat at around 2%–3%, while the conversion efficiency into gold ions increases linearly. Only at $I_0 > 2\times10^{21}$ W/cm^2, corresponding to ~20 J of laser energy, more energy is coupled to the bulk than to the contaminants. This is the regime best suited for heavy ion acceleration. The gold ions flux $dN/d\Omega$

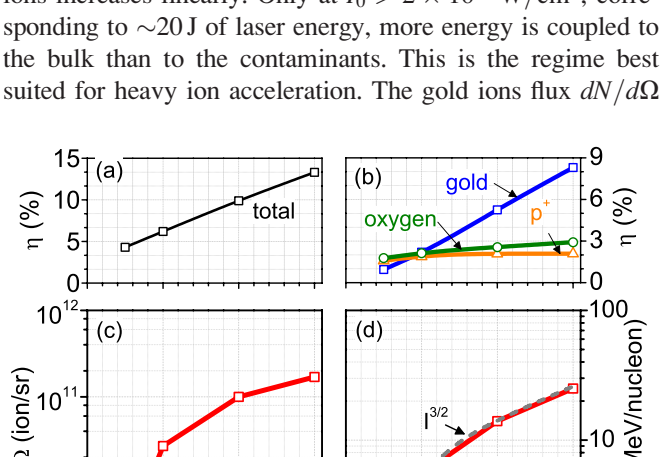

FIG. 9. Total conversion efficiency into ions (a), conversion efficiency into gold ions, oxygen ions and protons (b), gold ion flux, (c) and gold ion maximum energy per nucleon (d) versus laser intensity. Dashed line in panel (d): scaling of the maximum gold ion energy per nucleon with laser intensity. For panels (c) and (d), only ions with energy > 100 MeV within 10° half-angle from the target normal ($d\Omega = 0.095$ sr) are included. The relation between laser energy and peak intensity is $\varepsilon_{laser}(J) = 9\times I_0(\mathrm{W/cm^2})/10^{21}$.

and normalized maximum energy $(E/M)_{max}$ versus laser intensity are plotted in Figures 9(c) and 9(d), respectively. The ion flux sharply increases with laser intensity due to increased conversion efficiency, but then, it starts to saturate when all ions in the focal spot become accelerated. The maximum energy per nucleon increases with laser intensity (and energy) according to $(E/M)_{max} \sim I^{3/2}$. From Figure 9(d), we conclude that in order to generate gold ions with maximum normalized energy of few MeV/nucleon, the laser energy must be at least 10 J.

As it was pointed out in Section III, acceleration of ions from mid- and high-Z material is inherently inefficient. The numerical simulations presented in this section indicate that there are two general approaches to produce more energetic heavy ion beams: increase the charge-to-mass ratio, and improve the energy conversion efficiency. It is widely recognized that q/M plays a crucial role in the ion acceleration. Boosting q/M is therefore essential, and the potential to do so has been explored. Theoretically, for gold, the maximum charge-to-mass ratio is $(q/M)_{max} \cong 0.4$, provided the maximum charge is reached (fully stripped ions). In practice, however, it is lower: the average charge-to-mass ratio is only 0.25 (Figure 4(a)). Increasing the laser intensity from 5×10^{20} W/cm^2 to 3×10^{21} W/cm^2 did not increase appreciably q/M. The conclusion we drew is that regardless of the conditions, for gold ions, q/M is limited to about 0.25. Long pulses ($\sim$1 ps) allowing for collisional ionization to take place increased q/M only marginally. The only viable alternative is to put more energy into the heavy ions, which was accomplished by maximizing the energy absorption with an appropriate choice of foil thickness ($\ell \cong \ell_{skin}$) and manipulating the energy distribution among species in favor of Au with a proper choice of laser intensity ($I > 2 \times 10^{21}$ W/cm^2). This is the main reason to focus on the energy balance, which played central role for identifying a regime suitable for heavy ion acceleration.

V. NUMERICAL SIMULATION ISSUES PERTINENT TO HEAVY ION ACCELERATION

Finally, we discuss some simulation issues relevant to this work. The first one refers to modeling of relativistic laser pulses with high-Z material at solid density. In general, PIC simulations are prone to numerical instabilities at high electron densities typical for solids. The problem is exacerbated for plasmas containing highly charged ions. Compare, for example, targets made of Au and Al. They both have about the same neutral density, 6×10^{22} cm^{-3}, but the Au ions are highly charged. As a result, for high-Z materials, the electron density in the focal spot can become extremely large, exceeding $\sim$2000 times the critical density and causing numerical instabilities. The most notorious among them is the so-called "grid-heating."[41] The particle energy may artificially increase, unless the spatial resolution is kept below the Debye length or high-order interpolation schemes are implemented. To remedy the situation, we use an implicit discretization scheme for the Maxwell equations, which suppresses numerical instabilities.[33]

VI. SUMMARY AND CONCLUSIONS

Acceleration of heavy ions from thin ($<1\,\mu$m) foils in the RPA and TNSA regimes has been investigated theoretically by using a 2D PIC code for a laser system with short pulse duration (32 fs) and energy of up to 27 J. We established that there are extra limitations specific to heavy ion acceleration: (i) lower charge-to-mass ratio for heavy ions compared to light ions; (ii) smaller number of ions suitable for acceleration limited to the laser focal spot; (iii) two-stage process with ionization prevalent in the first stage during the raise of the laser pulse and acceleration during the fall of the laser pulse. Heavy ions can be accelerated only after the peak of the laser pulse; (iv) dense plasma ($>$2000 times the critical electron density) causing the so-called plasma mirror effect, in which most of the laser pulse is reflected and the energy coupled to the bulk is reduced; (v) competition with the contaminants on the foil surface, which can be overcome only at very high laser intensities. We also determined that the only practical approach to heavy ion acceleration is to improve the conversion efficiency into heavy ions by the choice of foil thickness and laser intensity. For ultrashort laser pulses ($<$40 fs), efficient acceleration is best realized for pulses with energy $>$20 J focused to a spot size $>5\,\mu$m at intensity $>10^{21}$ W/cm^2, and ultrathin foils with thickness $\ell \cong \ell_{skin} \cong$ 20–30 nm. The laser interaction with the foil generates two collimated counter-propagating ion beams from the bulk of the foil, along the laser propagation direction and in the backward direction. The forward accelerated beam has maximum normalized energy 25 MeV/nucleon and flux 2×10^{11} ions/sr.

ACKNOWLEDGMENTS

This work was performed with the support of the Air Force Office of Scientific Research under Grant No. FA9550-14-1-0282. G.M.P. would like to acknowledge the DoD HPC computing program at NRL.

[1]S. C. Wilks, A. B. Langdon, T. E. Cowan, M. Roth, M. Singh, S. Hatchett, M. H. Key, D. Pennington, A. MacKinnon, and R. A. Snavely, Phys. Plasmas **8**, 542 (2001).
[2]S. C. Wilks, W. L. Kruer, M. Tabak, and A. B. Langton, Phys. Rev. Lett. **69**, 1383 (1992).
[3]B. Qiao, M. Zepf, M. Borghesi, and M. Geissler, Phys. Rev. Lett. **102**, 145002 (2009).
[4]A. Macchi, S. Veghini, and F. Pegoraro, Phys. Rev. Lett. **103**, 085003 (2009).
[5]A. Henig, S. Steinke, M. Schnürer, T. Sokollik, R. Hörlein, D. Kiefer, D. Jung, J. Schreiber, B. M. Hegelich, X. Q. Yan, J. Meyer-ter-Vehn, T. Tajima, P. V. Nickles, W. Sandner, and D. Habs, Phys. Rev. Lett. **103**, 245003 (2009).
[6]B. Qiao, S. Kar, M. Geissler, P. Gibbon, M. Zepf, and M. Borghesi, Phys. Rev. Lett. **108**, 115002 (2012).
[7]N. P. Dover and Z. Najmudin, High Energy Density Phys. **8**, 170 (2012).
[8]T. Esirkepov, M. Borghesi, S. V. Bulanov, G. Mourou, and T. Tajima, Phys. Rev. Lett. **92**, 175003 (2004).
[9]A. Henig, D. Kiefer, K. Markey, D. C. Gautier, K. A. Flippo, S. Letzring, R. P. Johnson, T. Shimada, L. Yin, B. J. Albright, K. J. Bowers, J. C. Fernandez, S. G. Rykovanov, H.-C. Wu, M. Zepf, D. Jung, V. Kh. Liechtenstein, J. Schreiber, D. Habs, and B. M. Hegelich, Phys. Rev. Lett. **103**, 045002 (2009).
[10]L. O. Silva, M. Marti, J. R. Davies, R. A. Fonseca, C. Ren, F. S. Tsung, and W. B. Mori, Phys. Rev. Lett. **92**, 015002 (2004).

[11]L. Yin, B. J. Albright, B. M. Hegelich, and J. C. Fernández, Laser Part. Beams **24**, 291 (2006).
[12]I. J. Kim, K. H. Pae, C. M. Kim, H. T. Kim, J. H. Sung, S. K. Lee, T. J. Yu, I. W. Choi, C.-L. Lee, K. H. Nam, P. V. Nickles, T. M. Jeong, and J. Lee, Phys. Rev. Lett. **111**, 165003 (2013).
[13]L. Yin, B. J. Albright, B. M. Hegelich, K. J. Bowers, K. A. Flippo, T. J. T. Kwan, and J. C. Fernandez, Phys. Plasmas **14**, 056706 (2007).
[14]D. Jung, L. Yin, D. C. Gautier, H.-C. Wu, S. Letzring, B. Dromey, R. Shah, S. Palaniyappan, T. Shimada, R. P. Johnson, J. Schreiber, D. Habs, J. C. Fernandez, B. M. Hegelich, and B. J. Albright, Phys. Plasmas **20**, 083103 (2013).
[15]K. Ogura, M. Nishiuchi, A. S. Pirozhkov, T. Tanimoto, A. Sagisaka, T. Zh. Esirkepov, M. Kando, T. Shizuma, T. Hayakawa, H. Kiriyama, T. Shimomura, S. Kondo, S. Kanazawa, Y. Nakai, H. Sasao, F. Sasao, Y. Fukuda, H. Sakaki, M. Kanasaki, A. Yogo, S. V. Bulanov, P. R. Bolton, and K. Kondo, Opt. Lett. **37**, 2868 (2012).
[16]M. Nishiuchi, H. Sakaki, T. Zh. Esirkepov, K. Nishio, T. A. Pikuz, A. Ya. Faenov, I. Yu. Skobelev, R. Orlandi, H. Sako, A. S. Pirozhkov, K. Matsukawa, A. Sagisaka, K. Ogura, M. Kanasaki, H. Kiriyama, Y. Fukuda, H. Koura, M. Kando, T. Yamauchi, Y. Watanabe, S. V. Bulanov, K. Kondo, K. Imai, and S. Nagamiya, Phys. Plasmas **22**, 033107 (2015).
[17]B. M. Hegelich, B. Albright, P. Audebert, A. Blazevic, E. Brambrink, J. Cobble, T. Cowan, J. Fuchs, J. C. Gauthier, C. Gautier, M. Geissel, D. Habs, R. Johnson, S. Karsch, A. Kemp, S. Letzring, M. Roth, U. Schramm, J. Schreiber, K. J. Witte, and J. C. Fernández, Phys. Plasmas **12**, 056314 (2005).
[18]B. M. Hegelich, B. J. Albright, J. Cobble, K. Flippo, S. Letzring, M. Paffett, H. Ruhl, J. Schreiber, R. K. Schulze, and J. C. Fernandez, Nature **439**, 441 (2006).
[19]E. L. Clark, K. Krushelnick, M. Zepf, F. N. Beg, M. Tatarakis, A. Machacek, M. I. K. Santala, I. Watts, P. A. Norreys, and A. E. Dangor, Phys. Rev. Lett. **85**, 1654 (2000).
[20]J. Braenzel, A. A. Andreev, K. Platonov, M. Klingsporn, L. Ehrentraut, W. Sandner, and M. Schnürer, Phys. Rev. Lett. **114**, 124801 (2015).
[21]T. Zh. Esirkepov, S. V. Bulanov, K. Nishihara, T. Tajima, F. Pegoraro, V. S. Khoroshkov, K. Mima, H. Daido, Y. Kato, Y. Kitagawa, K. Nagai, and S. Sakabe, Phys. Rev. Lett. **89**, 175003 (2002).
[22]S. V. Bulanov and V. S. Khoroshkov, Plasma Phys. Rep. **28**, 453 (2002).
[23]P. McKenna, F. Lindau, O. Lundh, D. C. Carroll, R. J. Clarke, K. W. D. Ledingham, T. McCanny, D. Neely, A. P. L. Robinson, L. Robson, P. T. Simpson, C-G. Wahlstrom, and M. Zepf, Plasma Phys. Controlled Fusion **49**, B223 (2007).
[24]J. Schreiber, F. Bell, F. Gruner, U. Schramm, M. Geissler, M. Schnurer, S. Ter-Avetisyan, B. M. Hegelich, J. Cobble, E. Brambrink, J. Fuchs, P. Audebert, and D. Habs, Phys. Rev. Lett. **97**, 045005 (2006).
[25]V. P. Krainov and M. B. Smirnov, Phys. Rep. **370**, 237 (2002).
[26]B. M. Penetrante and J. N. Bardsley, Phys. Rev. A **43**, 3100 (1991).
[27]E. G. Gamaly, A. V. Rode, B. Luther-Davies, and V. T. Tikhonchuk, Phys. Plasmas **9**, 949 (2002).
[28]A. Macchi and C. Benedetti, Nucl. Instrum. Methods Phys. Res., Sect. A **620**, 41 (2010).
[29]A. Macchi, M. Borghesi, and M. Passoni, Rev. Mod. Phys. **85**, 751 (2013).
[30]T. Esirkepov, M. Yamagiwa, and T. Tajima, Phys. Rev. Lett. **96**, 105001 (2006).
[31]G. M. Petrov and J. Davis, Appl. Phys. B **96**, 773 (2009).
[32]S. S. Bulanov, A. Brantov, V. Yu. Bychenkov, V. Chvykov, G. Kalinchenko, T. Matsuoka, P. Rousseau, S. Reed, V. Yanovsky, K. Krushelnick, D. W. Litzenberg, and A. Maksimchuk, Med. Phys. **35**, 1770 (2008).
[33]G. M. Petrov and J. Davis, Phys. Plasmas **18**, 073102 (2011).
[34]G. M. Petrov and J. Davis, Commun. Comput. Phys. **16**, 599 (2014).
[35]G. M. Petrov, J. Davis, and Tz. Petrova, Plasma Phys. Controlled Fusion **51**, 095005 (2009).
[36]A. J. Kemp, R. E. W. Pfund, and J. Meyer-ter-Vehn, Phys. Plasmas **11**, 5648 (2004).
[37]J. Colgan, J. Abdallah, Jr., A. Ya. Faenov, S. A. Pikuz, E. Wagenaars, N. Booth, O. Culfa, R. J. Dance, R. G. Evans, R. J. Gray, T. Kaempfer, K. L. Lancaster, P. McKenna, A. L. Rossall, I. Yu. Skobelev, K. S. Schulze, I. Uschmann, A. G. Zhidkov, and N. C. Woolsey, Phys. Rev. Lett. **110**, 125001 (2013).
[38]A. P. L. Robinson, M. Zepf, S. Kar, R. G. Evans, and C. Bellei, New J. Phys. **10**, 013021 (2008).
[39]G. M. Petrov and J. Davis, Comput. Phys. Commun. **179**, 868 (2008).
[40]G. Lapenta and S. Markidis, Phys. Plasmas **18**, 072101 (2011).
[41]E. Cormier-Michel, B. A. Shadwick, C. G. R. Geddes, E. Esarey, C. B. Schroeder, and W. P. Leemans, Phys. Rev. E **78**, 016404 (2008).